Published in final edited form as:
Bo Pu Xue Za Zhi. 2014 March 1; 31(1): 116–132.

Magnetic Resonance Imaging of Stroke in the Rat

Guang-liang DING, **Michael CHOPP**, **Lian LI**, **Li ZHANG**, **Zheng-gang ZHANG**, **Qing-jiang LI**, and **Quan JIANG**
Department of Neurology, Henry Ford Hospital, Detroit 48202, USA

Abstract

Magnetic resonance imaging (MRI) is now a routine neuroimaging tool in the clinic. Throughout all phases of stroke from acute to chronic, MRI plays an important role to diagnose, evaluate and monitor the cerebral tissue undergoing stroke. This review provides a description of various MRI methods and an overview of selected MRI studies, with an embolic stroke model of rat, performed in the MRI laboratory of Department of Neurology, Henry Ford Hospital, Detroit, Michigan, US.

Keywords

MRI; stroke; rat

Introduction

Stroke is a leading cause of major adult disability and mortality around the world[1]. Cerebral arterial thrombosis is the predominant cause of ischemia which accounts for 85~90% cases of stroke[2]. The primary limitation of thrombolytic treatment is the risk of hemorrhagic transformation (HT) after receiving recombinant tissue plasminogen activator (rtPA) when the treatment is administered beyond the therapeutic window. Currently, only a small percentage of patients can receive rtPA, despite extending the treatment window from 3 to 4.5 h[3,4]. It is therefore important to develop alternate restorative therapies with a less restrictive window that can be applied to the vast majority of stroke patients[5,6]. Thus, advanced neuroimaging methodologies, to evaluate efficacy and risk of thrombolytic treatment and monitor the effect of restorative treatment, are required in the development of effective therapies for the management of stroke patients[7–9].

Magnetic resonance imaging (MRI) is now a routine neuroimaging tool in the clinic. Throughout all phases of stroke from acute to chronic, MRI plays an important role to diagnose, evaluate and monitor the cerebral tissue undergoing stroke. This review provides a description of various MRI methods and an overview of selected MRI studies performed in our laboratory on stroke in the rat[10].

MRI measurements were performed using a 7 T, 20 cm bore superconducting magnet (Magnex Scientific, Abingdon, UK) interfaced to a Bruker console (Bruker Company, Boston, MA, USA), with a 12 cm bore actively shielded gradient coil set capable of

Correspondence to: Guang-liang DING.

producing magnetic field gradients up to 200 mT/m. A birdcage radio-frequency (RF) coil was used as the transmitter and a surface coil as the receiver. Stereotaxic ear bars were utilized to minimize movement during the imaging procedure. During MRI measurements, the anesthesia of rats was maintained using a gas mixture of nitrous oxide (69%), oxygen (30%), and halothane (0.75~1.00%) or isoflorane (1.00~1.50%). Rectal temperature of rats was kept at 37 °C ± 1.0 °C using a feedback controlled water bath. The right femoral artery and vein of rats were cannulated with a PE-50 catheter for monitoring of blood pressure and gases (pH, partial pressure of oxygen [PO_2], carbon dioxide [PCO_2]), and for drug administration, when administered respectively.

All animal studies were performed in accordance with institutional guidelines for animal research under a protocol approved by the Institutional Animal Care and Use Committee (IACUC) of Henry Ford Hospital.

1 Magnetic Resonance Angiography (MRA)

MRA employs a three-dimension (3D) gradient echo imaging sequence with the first-order flow compensation[11]. The acquisition matrix is set as 256×192×64 for fitting the field-of-view (*FOV*) 32×32×16 mm^3 in Coronal-Head-Foot orientation. Repetition time (*TR*) and echo time (*TE*) are 50 ms and 4.5 ms, respectively. The 500 ms Gaussian RF pulse generates a flip angle of approximately 40 degrees. The resultant MRA image is reconstructed by maximum intensity projection (MIP) using 3D images.

Fig. 1 shows that rtPA and 7E3 $F(ab')_2$, a platelet glycoprotein (GP) IIb/IIIa receptor (GPIIb/IIIa) inhibitor, worked together to increase the efficiency of dissolving the embolus[12]. The MRA images demonstrated that right middle cerebral artery (MCA) was continuously occluded at 1 h, 24 h and 48 h after embolization in a control rat treated with rtPA alone (A1)~(A3). For the representative rat treated with combination of rtPA and 7E3 $F(ab')_2$, the MCA was occluded at 1 h and recanalized by 24 h after the onset of ischemia, as indicated by the MRA images (B1)~(B3). By 24 h after embolization, half the animals from the treated group (n=12) and two animals from the control group (n=10) had patent right branches of the MCA, the remaining animals (50% of treated group and 80% of control group) had occluded right MCA branches. No significant change was found in the MRA images from 24 h to 48 h for each group, e.g. Fig. 1A3 for occluded right MCA and Fig. 1B3 for patent right MCA at 48 h.

2 Arterial Spin Labeling (ASL)

The ASL technique is used for quantifying blood flow in cerebral tissue[13]. The adiabatic inversion of arterial water protons in the continuous ASL (cASL) sequence is accomplished via an axial gradient of ±0.3 kHz/mm[14], and a continuous wave (CW) RF pulse with power of approximately 0.3 kHz at a frequency offset of ±6 kHz. The CW RF pulse is hyperbolic secant shaped with 1 second duration and is employed as an adiabatic fast passage RF pulse, followed by a spin echo imaging sequence with *TR*/*TE* = 1 050 ms/ 20 ms. The labeling slab center is 2 cm upstream from the center of the imaging slice. To minimize the effects of magnetization transfer, only one central slice (0 offset, 1 mm slice thickness) is measured. In order to remove the asymmetry of gradient in the axial direction, an image average is

applied by switching around the gradient polarities. *FOV* is 32 mm×32 mm, matrix 64×64. The average number is 4. The cerebral blood flow (CBF) map (*f*-value) is calculated according to the ASL measurement[13].

CBF maps acquired using ASL from a rat subjected to embolic MCA occlusion and which received rtPA along with 7E3 $F(ab')_2$ are shown in Fig. 2. The rat exhibited low CBF in the ipsilateral hemisphere at 1 h after embolic stroke onset [Fig. 2(a)]. However, the 48 h CBF map showed an elevated cerebral perfusion of the ipsilateral cortex [Fig. 2(b)], since the right MCA was recanalized by 24 h after embolization in this combination treated rat. Measurement of microvascular patency, perfused by fluorescein isothiocyanate (FITC) dextran prior to euthanizing the animal at 48 h after stroke, indicated that combined rtPA and 7E3 $F(ab')_2$ therapy improved microvascular patency in the ipsilateral hemisphere of rat brain. As illustrated in Fig. 2(c), the cortical tissue of ipsilateral hemisphere exhibited bright microvessels because of microvessel fluorescence. The ipsilateral striatal tissue was darkened without any bright microvessels because of low blood perfusion, i.e. low fluorescence. Contralateral cortex and striatal tissue presented bright microvessels because of its normal blood perfusion [Fig. 2(d)]. CBF maps measured by spin labeling MRI matched the fluorescent immunohistochemical perfusion images in the rat at 48 h after stroke.

Combining MRA with CBF, we can analyze the secondary thrombosis after thrombolytic treatment of ischemic stroke. Atorvastatin (Lipitor®, Pfizer), a second- generation inhibitor of HMG-CoA (3-hydroxy-3-methylglutaryl-coenzyme A) reductase, reduces platelet activation. Thus, like 7E3 $F(ab')_2$ suppressing the aggregation of platelets, the beneficial effects of atorvastatin on coagulation inhibited secondary thrombosis downstream of the original thrombus and improved cerebral microvascular patency, as shown in Fig. 3. MRA images showed that right MCA was occluded at 2 h and recanalized at 24 h post embolization in both rats. However, in the saline treated rat, the CBF obtained at 24 h post stroke remained low in the ischemic territory of MCA. In contrast, the CBF at 24 h after stroke was elevated in the territory of right MCA in the rat treated at 4 h post stroke with rtPA and atorvastatin, which suggested that the effects of atorvastatin on coagulation and fibrinolysis inhibited secondary thrombosis and improved cerebral microvascular patency[12,15].

3 *T*1–, *T*2– and diffusion-weighted imaging (*T*1WI, *T*2WI and DWI)

Cerebral tissue undergoes time-dependent heterogeneous histopathological changes after stroke[16]. The longitudinal and transverse relaxation time constants T_1, T_2 and the apparent diffusion coefficient of water (ADC_w) of cerebral tissue exhibit different temporal profiles in ischemic brain[17]. ADC_w, derived from DWI, declines acutely after onset of ischemia, when cytotoxic edema of the ischemic cerebral tissue is triggered by energy failure[18]. With the cell membrane of ischemic tissue breakdown, ADC_w becomes elevated after the acute phase of ischemia when vasogenic edema occurs. Pseudo-normalization of ADC_w may appear. Cytotoxic edema can not be detected by T_1WI and T_2WI[19]. A delayed T_2 increase may identify vasogenic edema, while T_1 is increased after tissue destruction, edema or inflammation[20,21].

MRI maps of ADC_w, T_1 and T_2 obtained at 2 h, 24 h and 48 h post ischemia from a rat subjected to embolic stroke, are demonstrated in Fig. 4. On these images, T_1 and T_2 maps failed to detect ischemic lesions at 2 h after onset of stroke; while ADC_w map identified the infarction by 2 h post ischemia. However, areas with pseudo-normalization ADC_w values were present on the 24 h and 48 h images.

Thus, individual ADC_w, T_1 or T_2, can not coincidentally characterize ischemic brain tissue from acute to chronic. But, they may provide complementary information. Accordingly, a multiparametric (multispectral) nature of MRI data (ADC_w, T_1 and T_2) for tissue characterization may be possible to determine the histopathological stage of stroke more accurately than using any single MRI parameter. Iterative self-organizing data analysis technique algorithm (ISODATA), an objective unsupervised segmentation algorithm to minimize the need for human interaction and bias, incorporates multiparametric MRI images in an iterative, multistep process that assigns the input data into a set of clusters[22,23]. By inputing ADC_w, T_1 and T_2 maps, ISODATA deduces a theme map of signature, which represents the Euclidean distances between clusters[24,25]. In experimental studies, the signature is normalized by assigning white matter as 1 and cerebro-spinal fluid (CSF) in ventricles as 100, which quantitatively provides a single map to characterize cerebral tissue from acute to chronic phases of stroke.

ISODATA theme maps, as shown in Fig. 5, detected temporal profiles of ischemic lesion size, location and severity using colorful signatures at 2, 6, 24 and 48 h after onset of stroke in a control rat treated with saline at 4 h after embolization (upper row), and a treated rat received combination treatment of rtPA and 7E3 $F(ab')_2$ at 4 h post stroke (lower row), respectively. Comparing the theme maps of the animals, the increased rates of the mean values of signature and ischemic lesion size were apparently reduced in the combination treated rat starting from 24 h after stroke. These ischemic lesions identified by ISODATA matched the results on histological H&E stained sections (right column) obtained at 48 h post stroke.

The enlargement of brain ventricles is consistently documented after stroke, and may provide an objective, sensitive and quantitative measure of neuropathological change. It may also provide a common *in vivo* marker of the severity of clinical impairment associated with stroke. Ventricular enlargement is presumed to reflect atrophy of surrounding brain regions in human and animals. T_2WI can measure ventricular volume, and has been employed to monitor the dynamic expansion of ventricles after stroke to evaluate the therapeutic benefits of restorative treatment of stroke in animals[26].

4 Magnetization Transfer (MT)

Magnetization transfer exchange takes place between macromolecular and water protons. The macromolecular spins have a much broader absorption line shape than the liquid water spins, making them as much as 1 million times more sensitive to an appropriately placed off-resonance irradiation[27]. The preferential saturation of the macromolecular spins can be transferred to the liquid water spins via dipolar coupling and chemical exchange. The

longitudinal relaxation time constant T_1 for the two pools of spins under exchange reach an equilibrium value, T_{1sat}, during sufficient off-resonance irradiation.

An imaging variant of the Look-Locker (L-L) technique[28] is employed to quickly acquire dynamic images for fitting T_1 map. L-L sequence acquires a set of images that recover with a time constant T_1* from inversion toward a steady-state magnetization. T_1* is related to T_1, as well as to the tip-angle of the readout and the repetition time[12,29–31].

MT experiment employs two off-resonance CW saturation RF pulses inserted into the Look-Locker sequence, with the first inserted immediately prior to the inversion pulse and lasting 4.5 s and the second, 40 ms long, inserted after the signal acquisition. The offset frequency of saturation pulses is 8 kHz and the rotational frequency of B_1 field is 0.5 kHz. Inversion of the longitudinal magnetization is accomplished using a non-selective hyperbolic secant adiabatic pulse of 8 ms duration. During a single phase-encoding step, 32 small-tip-angle gradient-echo images (*TE* of 2.2 ms) for every slice are acquired at 80 ms intervals after each inversion. The total recovery time is 11 s. With this sequence, a slice of T_{1sat} map is obtained within 12 min (32×32 mm^2 *FOV*, 128×64 matrix, 2 mm slice thickness).

Employing T_{1sat} [Fig. 6(a)] and ADC_w [Fig. 6(b)] maps acquired at 2 h post stroke, a two-dimension (2D) cluster plot [Fig. 6(c)] of images, from a rat administered with rtPA and 7E3 $F(ab')_2$ at 4 h after onset of embolic stroke, predicted hemorrhage after ischemia. Using the combined conditions, 658 ms<T_{1sat}<807 ms and ADC_w<6.0×10^{-4} s/mm^2 [red frame in Fig. 6(c)], the cluster was transposed back onto the ADC_w map [Fig. 6(b)]. The cluster predicted three primary regions [red spots in Fig.6(b)] reflecting gross HT, which was verified in the histological section of rat brain at 48 h after onset of embolic MCAo [Fig. 6(d)][32].

5 DCE-MRI and DSC-MRI

Dynamic contrast enhanced MRI (DCE-MRI) generally focuses on the T_1 changes of tissue due to leakage after injection of contrast agent, e.g. Gd-DTPA. In contrast, dynamic susceptibility contrast MRI (DSC-MRI) primarily trace the T_2* changes of tissue containing blood vessels during the first pass of the injected contrast agent bolus. Thus, DSC-MRI produces perfusion parameters, such as CBV (cerebral blood volume), CBF, MTT (mean transit time) and TTP (time to peak). And DCE-MRI derives permeability parameters, such as blood-to-brain transfer constant, K_i, and blood volume of leakage, V_p. Recently, a dual-echo technique has been developed to simultaneously obtain both perfusion and permeability parameters via acquiring a short *TE* echo and a relative longer *TE* echo, which trace changes of T_1 and T_2*, respectively[33]. Since it needs high temporal resolution to repeat sequence for dynamically tracing the changes of T_1 and T_2*, echo-planar imaging (EPI), or other fast imaging techniques, are commonly employed. As a result, image quality of the derived perfusion and permeability parameter maps is limited.

Using L-L T_1 measurement, DCE-MRI procedure includes an L-L baseline scan, a bolus of 0.2 mmol/kg Gd-DTPA injection via a femoral vein, and then continuous ten L-L scans of post-contrast acquisition. With the L-L sequence, a set of five slices of T_1 maps (32×32 mm^2 *FOV*, 128×64 matrix, 2 mm slice thickness) is obtained in 2.5 min. Inversion of the longitudinal magnetization is accomplished using a non-selective hyperbolic secant

adiabatic pulse of 8 ms duration. During a single phase-encoding step, 24 small-tip-angle gradient-echo images (*TE* of 2.2 ms) for each slice are acquired at 50 ms intervals after each adiabatic inversion, and 5 different slice images are continuously acquired within the 50 ms interval. The total recovery time is 2 s. All ten dynamic sets of T_1 maps are obtained in 25 min with an interval of 3 s between any two temporal sets of T_1 maps[34].

For a rat with microscopic hemorrhage after ischemic stroke, K_i [Fig. 7(a)] and V_p [Fig. 7(b)] maps, obtained at 24 h post embolization, identified hemorrhagic regions compared to the 48 h histological H&E stained picture [Fig. 7(c)], where microscopic hemorrhage was shown in its magnified picture of 20× [Fig. 7(d)]. Microscopic hemorrhage was defined as blood evident only by microscopy, rather than the naked eye. During ischemia, breakdown of basal lamina with loss of astrocyte and endothelial cell contact subsequently increases permeability of Gd-DTPA molecule and cells (e.g. erythrocytes) [35,36]. A marked reduction in the basal lamina is present in regions of hemorrhage during focal ischemia[37]. This result indicated that DCE-MRI with Gd-DTPA was sensitive to blood-brain barrier (BBB) disruption. In addition, T_1WI images acquired pre- [Fig. 7(e)] and post-injection [Fig. 7(f)] of Gd-DTPA at 24 h after embolic MCAo show contrast enhancement, which indicated BBB disruption. However, contrast enhanced T_1WI did not provide quantitative permeability parameters.

6 Susceptibility weighted imaging (SWI) and *T*2*–weighted imaging (*T*2*WI)

Since deoxyhemoglobin, hemoglobin without bound oxygen molecules, is paramagnetic, lower level of blood oxygenation in venous vessels induces a difference in magnetic susceptibility between the blood and the surrounding extra-vascular tissue[38]. Choosing a *TE*, depending on main magnetic strength, to make anti-parallel phases between signals from blood and extra-vascular tissue in a voxel, the resultant signal is maximumally cancelled and then susceptibility weighted. Therefore, SWI is also referred to as BOLD (blood-oxygen-level dependent) venographic imaging. As in MRA, SWI also employs a 3D gradient echo imaging sequence with the full velocity compensation. But, instead of MIP, SWI creates minimum intensity projection (mIP). Specially, SWI combines both magnitude and phase images[39,40]. The filtered phase image is created as a mask, and magnitude image is then multiplied by this mask to increase the contrast in the magnitude image for objects, such as veins[41,42]. Based on the same mechanism, SWI is also sensitive to detect other objects with low magnitude and phase values, for example, iron, cells labeled with SPIO (superparamagnetic iron oxide) particles (feridex®, Bayer), and hemorrhage.

Local magnetic field inhomogeneity, induced e.g., by veins, SPIO labeled-cells or hemorrhage, causes relaxation process of protons modified and is characterized by T_2* (gradient echo) relaxation. Like SWI, thus, T_2*WI may detect these objects in brain tissue[43].

During angiogenesis after stroke, existing cerebral vessels expand and sprout. The BBB of newly-generated vessels during angiogenesis is not mature. These areas of permeable BBB can be detected by T_2*WI, as well as SWI, with hypointensity on T_2* map or SWI image, as shown in panels (a), (b) of Fig. 8, respectively. Matched with hypointensity curve on T_2*

map and SWI image, the warped histological endothelial barrier antigen (EBA) stained image [Fig. 8(c)] exhibited a line, where blood vessels were apparently enriched and were much clearer in the 10x microscope enlarged picture [Fig. 8(d)]. The warped histological image [Fig. 8(c)] was from the original EBA stained image [Fig. 8(e)], and T_2 map [Fig. 8(f)] was a referring image in warping procedure.

To distinguish angiogenesis from HT, dynamic observations for temporal profiles and additional MRI measurements for complementary information are required[44]. Hemorrhage generally occurs within the ischemic core, where the ischemia is the most severe; and angiogenesis primarily occurs along ischemic boundary zone. Most BBB damage in the embolic model of rat usually occurs prior to 48 h post stroke[45,46], while angiogenesis can be detected by MRI starting around two weeks after stroke. Fig. 9 exhibits T_2* evidence of angiogenesis in a representative sildenafil treated rat at 2 weeks(2 w) [Fig. 9(a), red arrow] and HT in a control rat at 1 w [Fig. 9(c)] after stroke, respectively. These T_2* maps could not distinguish angiogenesis from HT by themselves, regardless of shapes and locations of the hypointensity regions. However, The K_i maps, from the same rats as the T_2* maps, showed the different temporal patterns. Regional K_i was normal at 1 day(1 d) and increased at 2 w after stroke in the sildenafil treated rat [Fig. 9(b)]. Conversely, regional K_i was elevated early, a sign of BBB disruption, at 1 d and became “normal” at 1 w post stroke in the control rat [Fig. 9(d)]. These typical K_i evolution patterns, as complementary measurements, are helpful to distinguish angiogenesis from HT in brain after ischemia.

Using dynamic pattern, SWI can track SPIO particles labeled cells in studies of stroke with cell treatment[47]. As shown in Fig. 10, no intracisternally injected cells were found in the axial images of SWI obtained pre- [Fig. 10(a)] and 1 day(1 d) post-injection [Fig. 10(b)] of labeled cells. However, hypointensity spots in the image of SWI acquired 2 d after injection [Fig. 10(c)] appeared, indicating the arrival of SPIO particles labeled cells. With more cells gathering, the hypointensity area increased one more day after injection, and detected by SWI [Fig. 10(d)]. Therapeutic effects of cell transplantation can be evaluated after stroke in rat by combining SWI and ISODATA[48].

7 Diffusion tensor imaging (DTI) and Diffusion spectrum imaging (DSI)

DTI of MRI provides a means for delineating the anatomic connectivity of white matter (WM) pathways and can be used to detect pathologic tract disruption based on the movement of water. Water in WM moves more freely in the direction parallel to the tract than perpendicular to it, since axonal membranes and myelin restrict motion transverse to the tract. This diffusional directionality is known as fractional anisotropy (FA) and is directly correlated with histological markers of myelination. Furthermore, increased FA appears to correlate with WM tract integrity, while reduced FA is correlated with functional deficits[49–52].

In a representative sildenafil treated rat (see Fig. 11), FA map acquired 6 weeks(6 w) after stroke revealed axonal remodeling with elevated FA values (red arrow). DTI acquisition included one baseline of b=0 and six images of b=900 s/mm^2 at independent directions of diffusion gradients along *XZ*, *–XZ*, *YZ*, *Y–Z*, *XY* and *–XY*. Two 10 ms (δ) gradient pulses

separated 18 ms (Δ) on either side of the refocusing 180 degrees RF pulse were in sequence with *TR* of 1 500 ms and *TE* of 40 ms. The total time needed for DTI images with two averages was approximately 45 min. DTI fiber tracking at 6 w after stroke indicated reorganized high density (10.36 per voxel) and long fibers (8.82 mm) along ischemic boundary, which coincided with the increased FA value area. Histological picture of Bielschowsky's silver and Luxol fast blue (BLFB) stains for myelinated axons verified the DTI findings (red arrows), and axonal fibers were clear in the magnified picture (40x). In contrast, DTI demonstrated weakly elevated FA values, sparse (3.62 per voxel) and short fibers (2.62 mm) along the ischemic boundary in a control rat treated with saline. As in the treated rat, histological pictures were coincident with DTI images in the control rat[53].

FA is able to monitor well-reorganized white matter recovery after treatment of stroke in rats. However, FA may be unable to detect white matter reorganization when the fiber branches and fiber bundles cross, and FA merely expresses an overall lower value because of the assumption of a Gaussian diffusion inherent to the tensor model. Solving the orientation distribution function (ODF), which is used to describe the directionality of multimodal diffusion in regions with complex fiber architecture, permits more accurate detection of crossing fibers. This calculation involves a complex set of Q-space analysis, as generally termed as DSI. Q-ball is one *b*-value shell DSI with a higher resolution angular distribution[54], and diffusional kurtosis imaging (DKI) acquires multiple *b*-value shells but with less directions than Q-ball does to quantitatively measure the degree to which the diffusion displacement probability distribution deviates from a Gaussian form[55]. The apparent kurtosis coefficient (AKC) derived from DKI is superior to FA in the detection of white matter reorganization with prominent crossing axons[56]. However, solving the ODF requires high angular resolution MRI data. The more directions the MRI scan contains, the more accurate the produced ODF is, and the more time the MRI scan takes. Thus, very high angular resolution DSI is rarely employed for *in vivo* studies.

Q-ball was performed *ex vivo* using the same sequence as DTI, with b=900 s/mm^2 at 128 directions and one baseline. DTI-based DKI was performed ex vivo with b=500, 1 000, 1 500, 2 000 and 2 500 s/mm^2 at 29 directions. Using 4 averages, Q-ball and DKI took 27 and 31 h, respectively. For example, panels in Fig. 12 show results of an *ex vivo* experiment of rat. FA failed to detect crossing fibers with low values [Fig. 12(a)], while AKC did identify the crossing fibers with elevated values [Fig. 12(b), arrows]. Q-ball data [Fig. 12(c)] demonstrated crossing fibers in that region [Fig. 12(d)]. BLFB staining image [Fig. 12(e)] histologically confirmed the findings of AKC; fibers of axons along the lesion boundary were evident in the magnification panel [Fig. 12(f)].

In summary, we provide a table (Table 1) to list required scan time for various MRI sequences we have employed in our studies. MRI has provided multiple dynamic parameters to characterize changes of cerebral tissue with or without insult. And MRI has the potential to provide more parameters. Some of the parameters can be obtained using current MRI sequences. For instance, pH map can be deduced using magnetization transfer sequence by changing the frequency of off-resonance irradiation exactly to 3.5 ppm (for proton of –NH)[57,58]. With nano-particles of SPIO as contrast agent, a series of vascular parameters can be derived using T_2WI and T_2*WI[59]. In addition, combination of T_2WI and T_2*WI

sequences can produce oxygen extract factor of cerebral tissue[60]. MRI is an active field of investigation, and will likely provide additional powerful means to further investigation of stroke and neural injury.

Acknowledgments

Foundation item: National Institutes of Health, USA (NIH) P01 NS23393, NS42345; R01 NS38292, NS43324, NS48349, HL64766.

The author (G.D.) contributes this review as a memorial of Professor SHEN Lian-fang. The research presented in this review has been financially supported by grants from National Institutes of Health (NIH), United States. The authors acknowledge the major assistance received from many co-workers in the Department of Neurology, Henry Ford Hospital, Detroit, Michigan.

References

1. Broderick JP, William M. Feinberg lecture: Stroke therapy in the year 2025: Burden, breakthroughs, and barriers to progress[J]. Stroke. 2004; 35:205–211. [PubMed: 14671248]
2. Fieschi C, Argentino C, Lenzi GL, et al. Clinical and instrumental evaluation of patients with ischemic stroke within the first six hours[J]. J Neurol Sci. 1989; 91:311–321. [PubMed: 2671268]
3. NINDS. The national institute of neurological disorders and stroke rt-pa stroke study group: Tissue plasminogen activator for acute ischemic stroke[J]. N Engl J Med. 1995; 333:1 581–1 587. [PubMed: 7776987]
4. Hacke W, Kaste M, Bluhmki E, et al. Thrombolysis with alteplase 3 to 4.5 hours after acute ischemic stroke[J]. N Engl J Med. 2008; 359:1 317–1 329. [PubMed: 18596269]
5. Zhang ZG, Chopp M. Neurorestorative therapies for stroke: Underlying mechanisms and translation to the clinic[J]. Lancet Neurol. 2009; 8:491–500. [PubMed: 19375666]
6. Chopp M, Li Y, Zhang J. Plasticity and remodeling of brain[J]. J Neurol Sci. 2008; 265:97–101. [PubMed: 17610903]
7. Zhang ZG, Jiang Q, Zhang R, et al. Magnetic resonance imaging and neurosphere therapy of stroke in rat[J]. Ann Neurol. 2003; 53:259–263. [PubMed: 12557295]
8. Chopp M, Li Y. Treatment of stroke and intracerebral hemorrhage with cellular and pharmacological restorative therapies[J]. Acta Neurochir Suppl. 2008; 105:79–83. [PubMed: 19066087]
9. Chopp M, Zhang ZG, Jiang Q. Neurogenesis, angiogenesis, and MRI indices of functional recovery from stroke[J]. Stroke. 2007; 38:827–831. [PubMed: 17261747]
10. Zhang RL, Chopp M, Zhang ZG, et al. A rat model of focal embolic cerebral ischemia[J]. Brain Res. 1997; 766(1–2):83–92. [PubMed: 9359590]
11. Haase A, Frahm J, Matthaei D, et al. Flash imaging. Rapid nmr imaging using low flip-angle pulses[J]. J Mag Res. 1986; 67:258–266.
12. Ding G, Jiang Q, Zhang L, et al. Analysis of combined treatment of embolic stroke in rat with r-tpa and a gpiib/iiia inhibitor[J]. J Cereb Blood Flow Metab. 2005; 25:87–97. [PubMed: 15678115]
13. Williams D, Detre J, Leigh J, et al. Magnetic resonance imaging of perfusion using spin inversion of arterial water[J]. Proc Nat'l Acad Sci USA. 1992; 89:212–216. [PubMed: 1729691]
14. Dixon WT, Du LN, Faul DD, et al. Projection angiograms of blood labeled by adiabatic fast passag[J]. Magn Reson Med. 1986; 3:454–462. [PubMed: 3724425]
15. Ding G, Jiang Q, Li L, et al. Mri of combination treatment of embolic stroke in rat with rtpa and atorvastatin[J]. J Neurol Sci. 2006; 246:139–147. [PubMed: 16626754]
16. Jiang Q, Zhang RL, Zhang ZG, et al. Diffusion-, t_2-, and perfusion-weighted nuclear magnetic resonance imaging of middle cerebral artery embolic stroke and recombinant tissue plasminogen activator intervention in the rat[J]. J Cereb Blood Flow Metab. 1998; 18:758–767. [PubMed: 9663506]
17. Hoehn-Berlage M, Eis M, Back T, et al. Changes of relaxation times (t_1, t_2) and apparent diffusion coefficient after permanent middle cerebral artery occlusion in the rat: Temporal evolution,

regional extent, and comparison with histology[J]. Magn Reson Med. 1995; 34:824–834. [PubMed: 8598809]

18. Hoehn-Berlage M, Norris DG, Kohno K, et al. Evolution of regional changes in apparent diffusion coefficient during focal ischemia of rat brain: The relationship of quantitative diffusion NMR imaging to reduction in cerebral blood flow and metabolic disturbances[J]. JCereb Blood Flow Metab. 1995; 15:1 002–1 011. [PubMed: 7798326]
19. Knight RA, Dereski MO, Helpern JA, et al. Magnetic resonance imaging assessment of evolving focal cerebral ischemia. Comparison with histopathology in rats[J]. Stroke. 1994; 25:1 252–1 261. [PubMed: 8266354]
20. DeWitt LD, Kistler JP, Miller DC, et al. NMR-neuropathologic correlation in stroke[J]. Stroke. 1987; 18:342–351. [PubMed: 3564090]
21. Levesque I, Sled JG, Narayanan S, et al. The role of edema and demyelination in chronic t_1 black holes: A quantitative magnetization transfer study[J]. J Magn Reson Imaging. 2005; 21:103–110. [PubMed: 15666408]
22. Jacobs MA, Zhang ZG, Knight RA, et al. A model for multiparametric MRI tissue characterization in experimental cerebral ischemia with histological validation in rat: Part 1[J]. Stroke. 2001; 32:943–949. [PubMed: 11283395]
23. Soltanian-Zadeh H, Windham JP. Novel and general approach to linear filter design for contrast-to-noise ratio enhancement of magnetic resonance images with multiple interfering features in the scene[J]. J Electron Imaging. 1992; 1:171–182.
24. Ding G, Jiang Q, Li L, et al. Characterization of cerebral tissue by MRI map isodata in embolic stroke in rat[J]. Brain Res. 2006; 1084:202–209. [PubMed: 16566903]
25. Ding G, Jiang Q, Zhang L, et al. Multiparametric isodata analysis of embolic stroke[J]. J Neurol Sci. 2004; 223:135–143. [PubMed: 15337614]
26. Ding GL, Jiang Q, Li L, et al. Cerebral tissue repair and atrophy after embolic stroke in rat: An MRI study of erythropoietin therapy[J]. J Neurosci Res. 2010; 88(14):3 206–3 214.
27. Henkelman RM, Stanisz GJ, Graham SJ. Magnetization transfer in MRI: A review[J]. NMR Biomed. 2001; 14:57–64. [PubMed: 11320533]
28. Look DC, Locker DR. Time saving in measurement of NMR and epr relaxation times[J]. Rev Sci Instrum. 1970; 41:250–251.
29. Patlak CS, Blasberg RG. Graphical evaluation of blood-to-brain transfer constants from multiple-time uptake data. Generalizations[J]. J Cereb Blood Flow Metab. 1985; 5:584–590. [PubMed: 4055928]
30. Patlak CS, Blasberg RG, Fenstermacher JD. Graphical evaluation of blood-to-brain transfer constants from multiple- time uptake data[J]. J Cereb Blood Flow Metab. 1983; 3:1–7. [PubMed: 6822610]
31. Ewing JR, Jiang Q, Boska M, et al. T_1 and magnetization transfer at 7 tesla in acute ischemic infarct in the rat[J]. Magn Reson Med. 1999; 41:696–705. [PubMed: 10332844]
32. Ding G, Nagesh V, Jiang Q, et al. Early prediction of gross hemorrhagic transformation by noncontrast agent mri cluster analysis after embolic stroke in rat[J]. Stroke. 2005; 36:1 247–1 252.
33. Quarles CC, Gore JC, Xu L, et al. Comparison of dual-echo dsc-mri- and dce-MRI-derived contrast agent kinetic parameters[J]. Magn Reson Imaging. 30:944–953. [PubMed: 22617148]
34. Ding G, Jiang Q, Li L, et al. Detection of bbb disruption and hemorrhage by gd-dtpa enhanced MRI after embolic stroke in rat[J]. Brain Res. 2006; 1114:195–203. [PubMed: 16950236]
35. Haring HP, Berg EL, Tsurushita N, et al. E-selectin appears in nonischemic tissue during experimental focal cerebral ischemia[J]. Stroke. 1996; 27(8):1 386–1 391. (discussion 1 391–1 392). [PubMed: 8553382]
36. Okada Y, Copeland BR, Mori E, et al. P-selectin and intercellular adhesion molecule-1 expression after focal brain ischemia and reperfusion[J]. Stroke. 1994; 25:202–211. [PubMed: 7505494]
37. Hamann GF, Okada Y, del Zoppo GJ. Hemorrhagic transformation and microvascular integrity during focal cerebral ischemia/reperfusion[J]. J Cereb Blood Flow Metab. 1996; 16:1 373–1 378. [PubMed: 8530541]
38. Yablonskiy DA, Haacke EM. Theory of NMR signal behavior in magnetically inhomogeneous tissues: The static dephasing regime[J]. Magn Reson Med. 1994; 32:749–763. [PubMed: 7869897]

39. Haacke EM, Mittal S, Wu Z, et al. Susceptibility-weighted imaging: Technical aspects and clinical applications, part 1[J]. AJNR Am J Neuroradiol. 2009; 30:19–30. [PubMed: 19039041]
40. Mittal S, Wu Z, Neelavalli J, et al. Susceptibility-weighted imaging: Technical aspects and clinical applications, part 2[J]. AJNR Am J Neuroradiol. 2009; 30:232–252. [PubMed: 19131406]
41. Reichenbach JR, Barth M, Haacke EM, et al. High-resolution MR venography at 3. 0 tesla[J]. J Comput Assist Tomogr. 2000; 24:949–957. [PubMed: 11105717]
42. Reichenbach JR, Venkatesan R, Schillinger DJ, et al. Small vessels in the human brain: MR venography with deoxyhemoglobin as an intrinsic contrast agent[J]. Radiology. 1997; 204:272–277. [PubMed: 9205259]
43. Haacke EM, Cheng NY, House MJ, et al. Imaging iron stores in the brain using magnetic resonance imaging[J]. Magn Reson Imaging. 2005; 23:1–25. [PubMed: 15733784]
44. Ding G, Jiang Q, Li L, et al. Angiogenesis detected after embolic stroke in rat brain using magnetic resonance T_2^*wi[J]. Stroke. 2008; 39:1 563–1 568. [PubMed: 18006859]
45. Zhang L, Zhang RL, Wang Y, et al. Functional recovery in aged and young rats after embolic stroke: Treatment with a phosphodiesterase type 5 inhibitor[J]. Stroke. 2005; 36:847–852. [PubMed: 15746452]
46. Jiang Q, Zhang RL, Zhang ZG, et al. Magnetic resonance imaging characterization of hemorrhagic transformation of embolic stroke in the rat[J]. J Cereb Blood Flow Metab. 2002; 22:559–568. [PubMed: 11973428]
47. Li L, Jiang Q, Ding GL, et al. Effects of route administration on migration and distribution of neural progenitor cells transplanted into rats with focal cerebral ischemia, an mri study[J]. J Cereb Blood Flow Metab. 2010; 30:653–662. [PubMed: 19888287]
48. Li L, Jiang Q, Zhang L, et al. Ischemic cerebral tissue response to subventricular zone cell transplantation measured by iterative self-organizing data analysis technique algorithm[J]. J Cereb Blood Flow Metab. 2006; 26:1 366–1 377. [PubMed: 15959458]
49. Beaulieu C. The basis of anisotropic water diffusion in the nervous system - a technical review[J]. NMR Biomed. 2002; 15:435–455. [PubMed: 12489094]
50. Mori S, van Zijl PC. Fiber tracking: Principles and strategies - a technical review[J]. NMR Biomed. 2002; 15:468–480. [PubMed: 12489096]
51. Sotak CH. The role of diffusion tensor imaging in the evaluation of ischemic brain injury - a review[J]. NMR Biomed. 2002; 15:561–569. [PubMed: 12489102]
52. Watanabe T, Honda Y, Fujii Y, et al. Three-dimensional anisotropy contrast magnetic resonance axonography to predict the prognosis for motor function in patients suffering from stroke[J]. J Neurosurg. 2001; 94:955–960. [PubMed: 11409525]
53. Ding G, Jiang Q, Li L, et al. Magnetic resonance imaging investigation of axonal remodeling and angiogenesis after embolic stroke in sildenafil-treated rats[J]. J Cereb Blood Flow Metab. 2008; 28:1 440–1 448. [PubMed: 17684514]
54. Tuch DS, Reese TG, Wiegell MR, et al. Diffusion MRI of complex neural architecture[J]. Neuron. 2003; 40:885–895. [PubMed: 14659088]
55. Jensen JH, Helpern JA, Ramani A, et al. Diffusional kurtosis imaging: The quantification of non-gaussian water diffusion by means of magnetic resonance imaging[J]. Magn Reson Med. 2005; 53:1 432–1 440.
56. Jiang Q, Qu C, Chopp M, et al. MRI evaluation of axonal reorganization after bone marrow stromal cell treatment of traumatic brain injury[J]. NMR Biomed. 2011; 24:1 119–1 128. [PubMed: 21259366]
57. Zhou J, Payen JF, Wilson DA, et al. Using the amide proton signals of intracellular proteins and peptides to detect ph effects in MRI[J]. Nat Med. 2003; 9:1 085–1 090.
58. Sun PZ, Zhou J, Sun W, et al. Detection of the ischemic penumbra using ph-weighted MRI[J]. J Cereb Blood Flow Metab. 2007; 27:1 129–1 136. [PubMed: 16685255]
59. Jensen JH, Chandra R. MR imaging of microvasculature[J]. Magn Reson Med. 2000; 44:224–230. [PubMed: 10918321]
60. An H, Lin W. Quantitative measurements of cerebral blood oxygen saturation using magnetic resonance imaging[J]. J Cereb Blood Flow Metab. 2000; 20:1 225–1 236.

Biography

Biography: DING Guang-liang(1963-), male, born in Jiangsu, PhD., his research focuses on MRI, Tel: +01-313-916-2620, gdingl@hfhs.org.

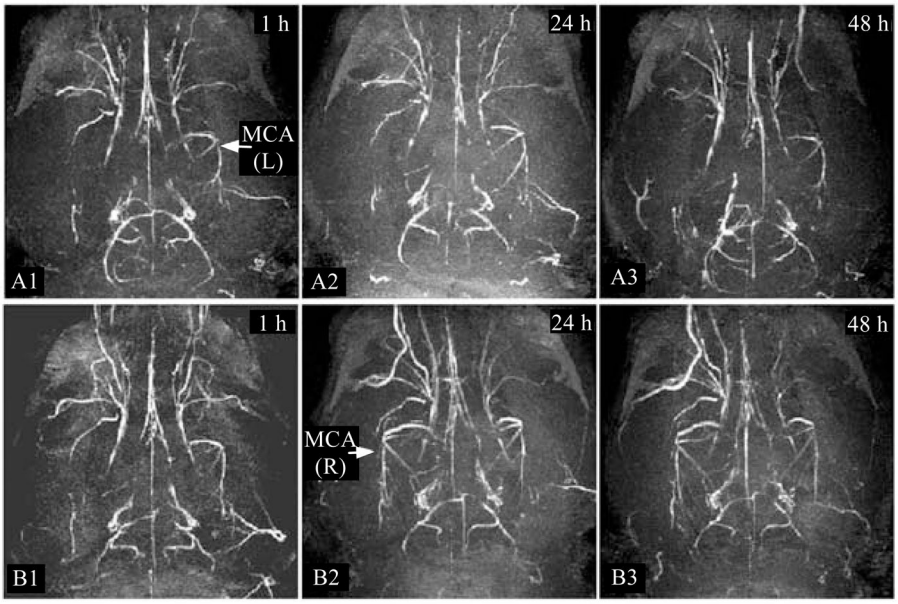

Fig. 1.

Right MCA was continuously occluded at 1 h (A1), 24 h (A2) and 48 h (A3) after embolization in a control rat treated with rtPA alone. In a rat treated with combination of rtPA and 7E3 $F(ab')_2$, the right MCA was occluded at 1 h (B1), but recanalized by 24 h (B2, B3) after the onset of ischemia

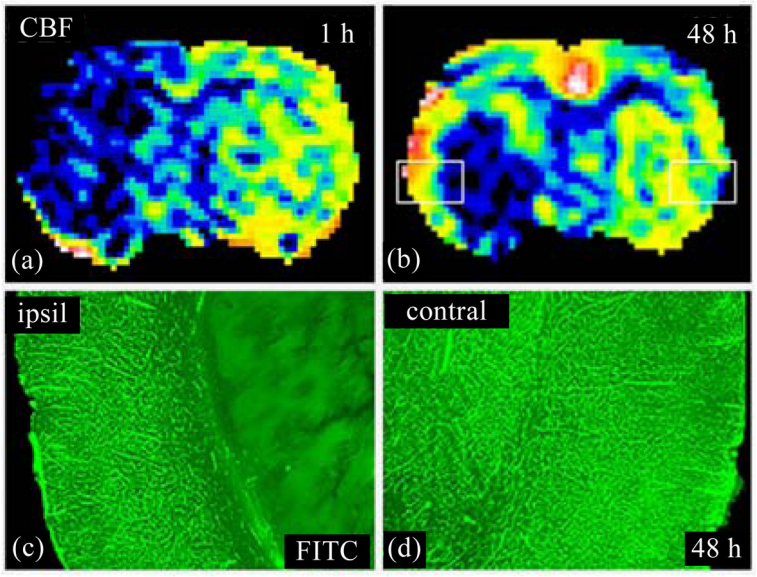

Fig. 2.

CBF was low in the ipsilateral hemispheres at 1 h after stroke onset (a). The CBF map obtained at 48 h after stroke showed an elevated cerebral perfusion of the ipsilateral cortex (b). The ipsilateral cortical or striatal tissue exhibited bright or dark microvessels (c), because of high or low blood perfusion, respectively. Contralateral cortex and striatal tissue presented bright microvessels because of its normal blood perfusion (d)

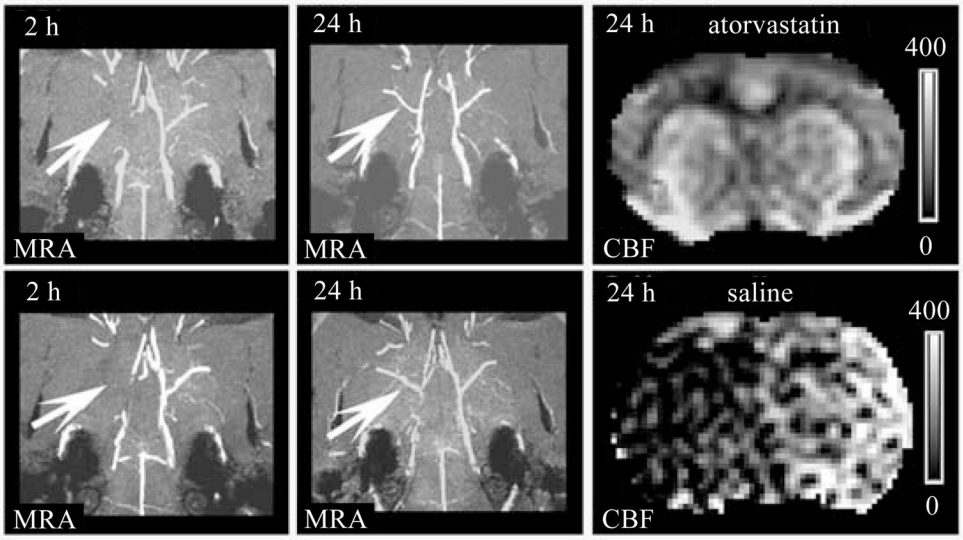

Fig. 3.

Right MCA was occluded at 2 h and recanalized at 24 h post embolization in both rats (arrows in MRA). The CBF at 24 h post stroke of saline treated rat remained low in the ischemic territory of MCA. In contrast, the 24 h CBF was elevated in the territory of right MCA in the rat administrated at 4 h post stroke with rtPA and atorvastatin

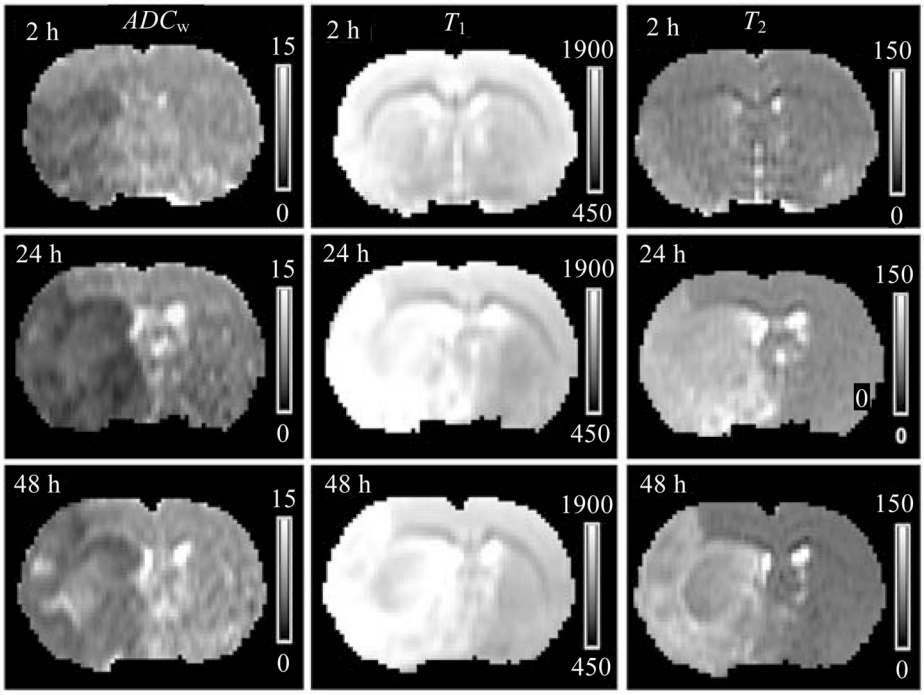

Fig. 4.

From an embolic stroke rat, ADC_w, T_1 and T_2 maps were obtained at 2 h, 24 h and 48 h post ischemia. On these maps, T_1 and T_2 maps failed to detect ischemic lesions at 2 h after onset of stroke; while ADC_w map identified the infarction by 2 h post ischemia. However, areas with pseudo-normalization values exhibited on 24 h and 48 h ADC_w maps

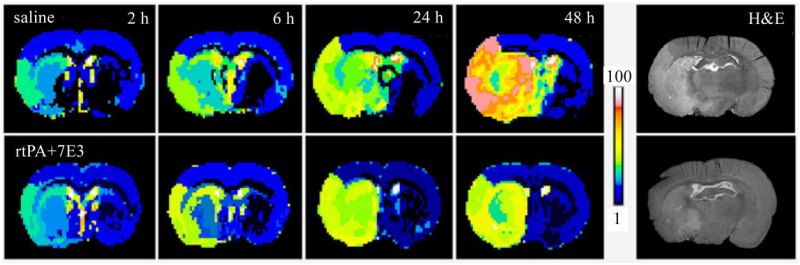

Fig. 5.

Theme maps of ISODATA detected size, location and severity of the ischemic tissue at 2, 6, 24 and 48 h after onset of stroke in rats. The upper row maps exhibited the quick increases of ischemic lesion size and severity from 2 to 48 h in a control rat, treated with saline at 4 h post stroke. For a rat received combination treatment of rtPA and 7E3 $F(ab')_2$ at 4 h post stroke, the ISODATA theme maps, the lower row, presented a reduced increase rates of ischemic lesion size and severity from 2 to 48 h after stroke. Ischemic lesions identified by ISODATA matched the histological results (H&E stain, right column) obtained at 48 h post stroke

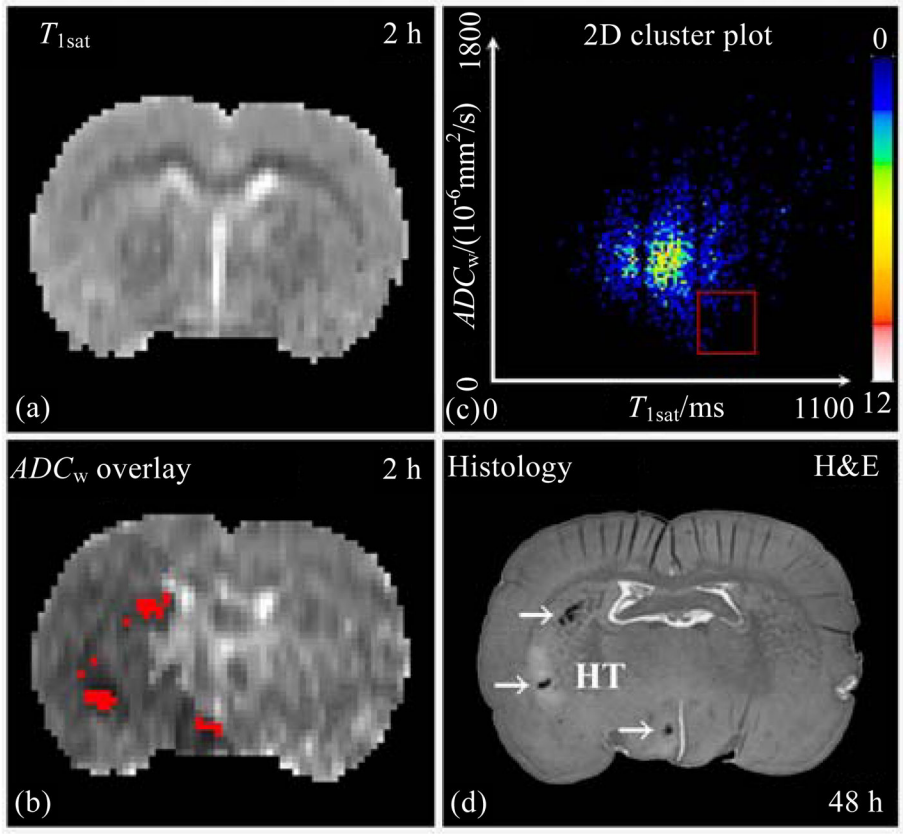

Fig. 6.

Employing T_{1sat} (a) and ADC_w (b) maps acquired at 2 h post stroke, a 2D cluster was plotted (c). The overlay onto the ADC_w map [(b), red spots] was the cluster with 658 ms< T_{1sat}<807 ms and ADC_w<6.0×10^{-4} s/mm^2 [red frame in (c)]. This cluster [red spots in (b)] predicted three primary regions for gross HT, which was verified in the histological H&E stained section of rat brain at 48 h after onset of embolic MCAo (d)

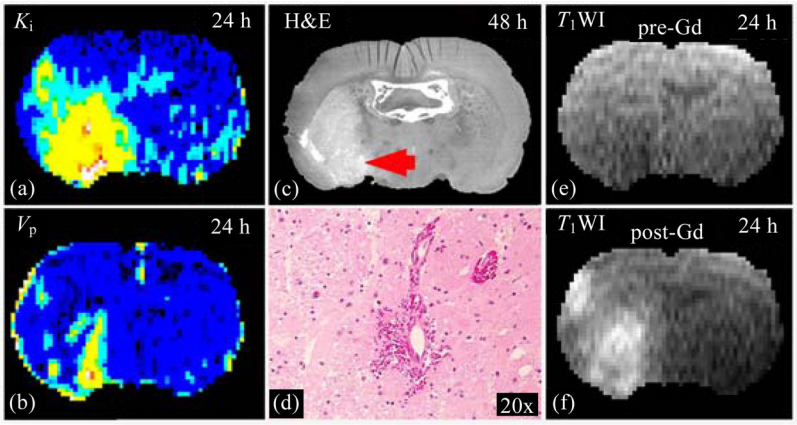

Fig. 7.

K_i (a) and V_p (b) maps, obtained at 24 h post embolization, exhibited elevated values at a region where histological H&E stained section (c), obtained at 48 h after stroke, identified the microscopic hemorrhage, which can be seen under microscopy with 20 times magnification (d). Due to BBB disruption, T_1WI images acquired pre- (e) and post-injection (f) of Gd-DTPA at 24 h after MCAo showed contrast enhancement

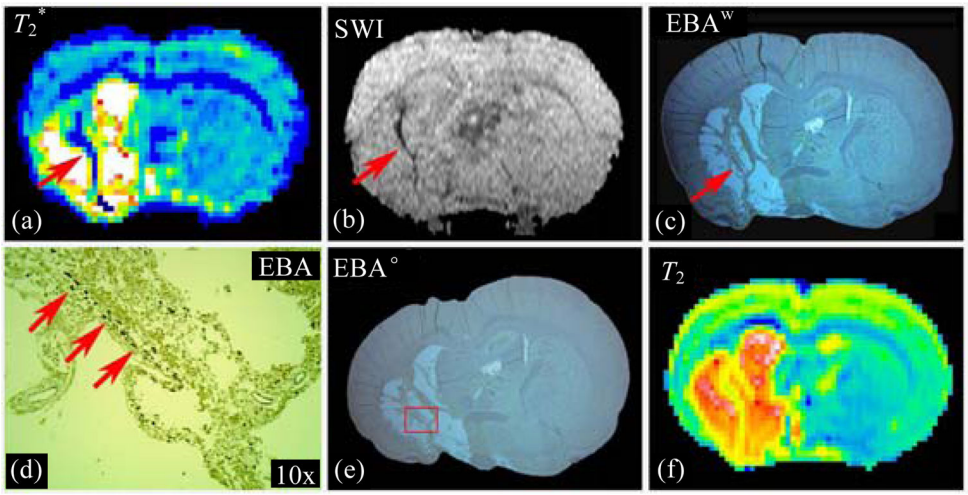

Fig. 8.

Both T_2* map (a) and SWI image (b) detected angiogenesis in rat brain after stroke as hypointensity area along ischemic boundary zone. Warped EBA stained image (c) exhibited a line with enriched blood vessels (d), which matched with the hypointensity curve on T_2* and SWI images. The magnified picture (d) was from the original EBA stained image (e). T_2 map (f) was a referred image in warping procedure

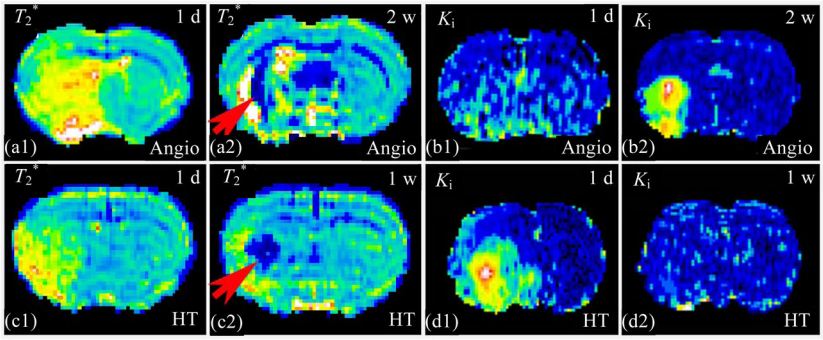

Fig. 9.

T_2* evidences of angiogenesis (a) and hemorrhage (c) after stroke could not be distinguished by themselves, excluding shapes and locations. The K_i maps, from the same rats as T_2* maps, showed the different temporal patterns. Regional K_i was normal at 1 d and increased at 2 w after stroke indicating angiogenesis (b). Conversely, regional K_i early elevated, a sign BBB disruption, at 1 d and became “normal” at 1 w post stroke, indicating HT (d). Combining complementary measurements would be helpful to distinguish angiogenesis from HT in brain after ischemia

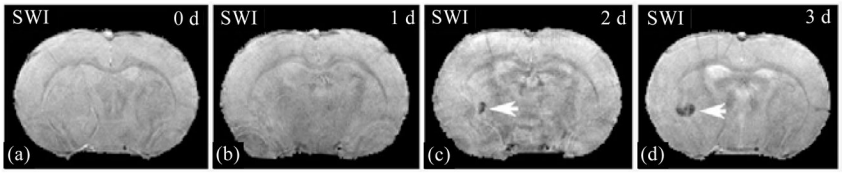

Fig. 10.

No feridex labeled cells, intracisternally administrated 24 h after stroke, were found in the axial SWI images of pre-injection (a) and 1 d post-injection (b). Hypointensity spot in SWI image acquired 2 d after injection (c) appeared, indicating the arrival of the labeled cells. The hypointensity area increased with more cells gathering (d)

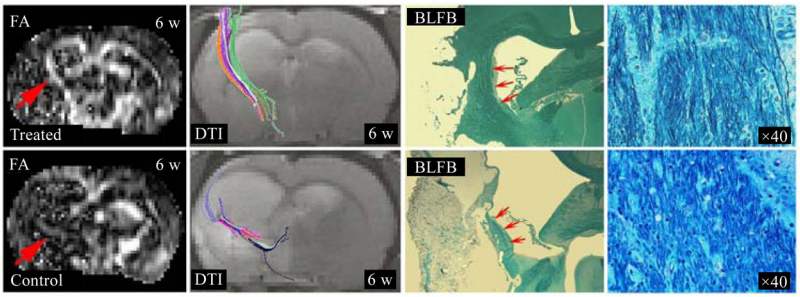

Fig. 11.

In a sildenafil treated rat, FA map acquired 6 w after stroke revealed axonal remodeling with higher FA values (red arrow). DTI tracked reorganized high density and long fibers along ischemic boundary, which coincided with the increased FA value area. BLFB staining section verified the DTI findings (red arrows), axonal fibers were much clearer in the magnified picture (40x). In a saline treated rat, DTI demonstrated weakly elevated FA values, sparse and short fibers along ischemic boundary, and BLFB pictures were coincident with DTI images

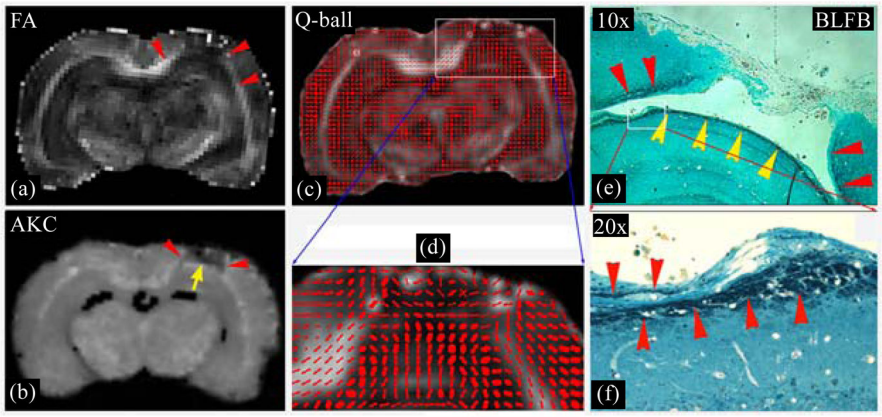

Fig. 12.

In an *ex vivo* experiment of rat, FA map, with low values, failed to detect crossing fibers (a). AKC identified the crossing fibers with elevated values [(b), arrows]. Q-ball image (c), with the enlarged part (d), demonstrated fibers cross in that region. BLFB staining image (e) coincided with AKC, fibers of axon along the lesion boundary were evident in the magnification panel (f)

Table 1

Scan times of various MRI measurements

Method	Matrix	*TR*(s)	*TE*(ms)/*b*(×100 s/mm^2)	Average	Scan time
MRA	256×192×64	0.05	4.5	1	~10 min
ASL	64×64, 1×1 mm	1.05	20	4	~18 min
T_1WI	128×128, 13×1 mm	0.5	15	2	~2 min
T_2WI	128×64, 13×1 mm	4.5	(15, 30, 45, 60, 75, 90)	1	~5 min
DWI	128×64, 13×1 mm	1.5	40 / (0, 6, 12)	1	~5 min
MT	128×64, 1×2 mm	11	7	1	~12 min
L-L	128×64, 5×2 mm	2	2.2	1	~2.5 min
SWI	256×256×96	0.03	10	1	~12 min
T_2*WI	128×64, 13×1 mm	4.5	(3, 6, 9, 12, 15, 18)	1	~5 min
DTI	128×128, 13×1 mm	1.5	40 / (0, 9×6)	2	~45 min
Q-ball	128×128, 13×1 mm	1.5	40 / (0, 9×128)	4	~27 h
DKI	128×128, 13×1 mm	1.5	40 / (0, {5,10,15,20,25}×29)	4	~31 h